Photoacoustics 12 (2018) 67–74

Contents lists available at ScienceDirect

Photoacoustics

journal homepage: www.elsevier.com/locate/pacs

Research article

Photoacoustic imaging for monitoring periodontal health: A first human study

Colman Moore[a], Yuting Bai[a], Ali Hariri[a], Joan B. Sanchez[b], Ching-Yu Lin[a], Sreenivas Koka[c,d], Parish Sedghizadeh[b], Casey Chen[b], Jesse V. Jokerst[a,e,f,*]

[a] Department of NanoEngineering, University of California, San Diego, 9500 Gilman Drive. La Jolla, CA, 92092, USA
[b] Herman Ostrow School of Dentistry, University of Southern California, 925 West 34th Street, Los Angeles, CA, 90089, USA
[c] School of Dentistry, University of California, Los Angeles, 714 Tiverton Ave, Los Angeles, CA, 90024, USA
[d] Koka Dental Clinic, 8031 Linda Vista Rd, San Diego, CA, 92111, USA
[e] Materials Science Program, University of California, San Diego, 9500 Gilman Drive. La Jolla, CA, 92092, USA
[f] Department of Radiology, University of California, San Diego, 9500 Gilman Drive. La Jolla, CA, 92092, USA

ARTICLE INFO

Keywords:
Photoacoustic imaging
Periodontal disease
Diagnosis
Gingival thickness
Pocket depth
Periodontal charting
Melanin nanoparticles

ABSTRACT

The gold-standard periodontal probe is an aging tool that can detect periodontitis and monitor gingival health but is highly error-prone, does not fully characterize the periodontal pocket, and causes pain. Photoacoustic imaging is a noninvasive technique that can address these limitations. Here, a range of ultrasound frequencies between 16–40 MHz were used to image the periodontium and a contrast medium based on cuttlefish ink was used to label the pockets. A 40 MHz ultrasound frequency could spatially resolve the periodontal anatomy, including tooth, gum, gingival margin, and gingival thickness of tooth numbers 7–10 and 22–27. The photoacoustic-ultrasound measurements were more precise (0.01 mm) than those taken with physical probes by a dental hygienist. Furthermore, the full geometry of the pockets could be visualized with relative standard deviations of 10% (n = 5). This study shows the potential for non-invasive monitoring of periodontal health with photoacoustic-ultrasound imaging in the dental clinic.

1. Introduction

Periodontitis affects nearly 50% of Americans and exerts both local and systemic effects on the body [1,2]. These range from mild discomfort to debilitating pain, tooth loss, and excessive activation of the immune system [3–5]. In fact, studies have identified the chronic inflammation from periodontitis as a risk factor for conditions such as cardiovascular disease [6–8], cancer [9], and dementia [10,11]. Thus, it is critical to diagnose periodontal disease early while the symptoms are mild and reversible [12].

The current metrics for monitoring periodontal health include attachment level, probing depth, bone loss, mobility, recession, and degree of inflammation [13]. The gold standard for quantifying periodontitis progression is the measurement of clinical attachment loss with a periodontal probe. This tool provides a numerical metric that reflects the degree of apical epithelial attachment measured from the gingival margin and is critical for disease staging [14].

However, the periodontal probe is a relatively unsophisticated tool that suffers from poor reproducibility [14,15]. These errors are attributed to the significant variation in probing force between operators, which can vary across multiple orders of magnitude [16]. Physical probing can penetrate inflamed tissue leading to patient discomfort, bleeding, and inaccurate measurements [5,17]. The probe can also only measure depth at the point of insertion—with no information on the full width or contour of the pocket. Furthermore, the benefit of traditional probing around dental implants is abrogated due to the implant threads that impede probe penetration along the implant surface [18,19]. This limits clinical assessment of these tissues potentially leading to peri-implantitis [20,21].

We recently described an approach that uses photoacoustic imaging to potentially address these issues [22]. Photoacoustic imaging is a hybrid imaging modality that combines visible and near infrared excitation with acoustic detection [23–26]. It extends the utility of ultrasound by enabling contrast based on optical absorption [27,28]. Traditional ultrasound operates under the principle of “sound in, sound out”, but photoacoustic imaging shifts this concept to “light in, sound out” [29]. Here, a near infrared laser excites a light-absorbing target. The target then undergoes spatially confined heating followed by

* Corresponding author at: Department of NanoEngineering, University of California, San Diego, 9500 Gilman Drive. La Jolla, CA, 92092, USA.
E-mail address: jjokerst@ucsd.edu (J.V. Jokerst).

https://doi.org/10.1016/j.pacs.2018.10.005
Received 8 August 2018; Received in revised form 28 October 2018; Accepted 29 October 2018
Available online 01 November 2018

thermoelastic expansion. This generates wideband acoustic waves that can be detected with ultrasound transducers for image generation. The clinical applications of photoacoustic imaging are growing; some recent examples include endogenous imaging of inflammatory arthritis, non-invasive assessment of Crohn's Disease, and diagnosis of vascular malformations [30–35]. Though photoacoustic-ultrasound (PA-US) signal can be limited by tissue penetration, it has two significant advantages over radiography, the most common dental imaging modality [36]: (1) it can image soft tissue; and (2) it does not use ionizing radiation. Additionally, the surfaces of hard tissues such as bone [37] and teeth [38] can be imaged.

Our previous report demonstrated the first application of photoacoustics for periodontal health and used a biocompatible oral contrast agent based on food-grade cuttlefish ink [22]. That work utilized swine models and imaged nearly 40 teeth to validate the method. While bias values relative to gold standard were low (< 0.2 mm), unresolved questions remained about its clinical utility. Here, we show that photoacoustic-ultrasound can image both the full depths and geometries of pockets in healthy human adults for non-invasive monitoring of gingival health after local irrigation of the pocket with contrast media.

2. Materials and methods

2.1. Reagents and equipment

Cuttlefish ink was purchased from Conservas de Cambados and contained ink, water, salt, and sodium carboxymethyl cellulose. Phosphate-buffered saline tablets were purchased from Sigma-Aldrich. Ultrasound gel was obtained from Next Medical Products. PA-US images were taken with a laser-integrated high frequency ultrasound system from Visualsonics (Vevo LAZR). A medical head immobilizer was purchased from DealMed. Disposable dental cheek retractors were obtained from Url Dental.

Contrast agent solutions were prepared individually from stock solutions of cuttlefish ink for each imaging experiment. Stock cuttlefish ink solutions (50% w/v in 0.1 M PBS) were aliquoted and refrigerated. To prepare the contrast agent, an aliquot was diluted and mixed with corn starch to a final solution containing 5% ink w/v and 2% corn starch. It was briefly heated to boiling to achieve homogeneity. The spherical melanin nanoparticles within the contrast agent were previously characterized with transmission electron microscopy, which indicated a mean particle size of 125 nm from 500 nanoparticles; and dynamic light scattering, which showed a hydrodynamic radius of 266 nm with a polydispersity index of 0.116 [22]. It is a food-grade material and was approved for human use by the Institutional Review Board (IRB). Human subject exclusion criteria included a shellfish allergy or a kosher diet.

2.2. Volunteer recruitment

This case study enrolled a healthy 22-year old adult female with good oral hygiene. All work with human subjects was approved by the UCSD IRB and conducted according the ethical standards set forth by the IRB and the Helsinki Declaration of 1975. The participant gave written informed consent and teeth 7–10, 22–27 were imaged.

2.3. Periodontal probe measurements

Pockets were measured with the Williams and Marquis probes [39] by a licensed periodontist. The measurements were performed at the distobuccal, mesiobuccal, and buccal sites according to clinical convention [40]. For distal and mesial measurements, the probe was inserted at a 10° angle at the interproximal space between adjacent teeth. The buccal measurements were collected at the deepest point observed after walking the probe across the width of the pocket. Per standard clinical practice, measurements were rounded up to the nearest integer. For the Williams probe, all measurements < 2 mm were recorded as 2 mm. For the Marquis probe, readings within the 3 mm intervals were estimated to be either in the lower 1.5 mm or upper 1.5 mm range and then rounded up to the nearest integer.

2.4. Pocket labeling

The subgingival pockets were labelled with ~8 μL of contrast agent per tooth. A micropipette with a sterile 2–20 μL tip was placed in contact with the gingival sulcus and used to irrigate the region with contrast agent. Following imaging, the contrast agent was removed from the pockets by rinsing the mouth with water or gentle tooth brushing (< 10 s).

2.5. Imaging procedure

Photoacoustic imaging was performed by pulsing light through two optical fiber bundles integrated with both sides of a rectangular, linear array transducer. The laser excitation (Q-switched Nd:YAG) used 5 ns pulses at 20 Hz (6 Hz frame rate). The ultrasound resolution was controlled by changing between three transducers: LZ-201 (center frequency = 16 MHz), LZ-250 (center frequency = 21 MHz), and LZ-550 (center frequency = 40 MHz). Typical gains were 15 dB for photoacoustic signal and 10 dB for ultrasound. The subject and operator both wore near-infrared protective laser goggles during experiments. The subject was seated in front of the imaging system and rested their chin on a flat surface in front of the transducer. The subject wore dental cheek retractors and a medical head immobilizer to reduce movements that contribute to motion-based imaging artifacts. A layer of ultrasound gel was applied to the transducer, which was adjusted to 1 cm from the tooth. The 680 nm laser was initialized, and the stepper motor was scanned 17 mm (0.076 mm step size) to obtain a 3D PA-US image via maximum intensity projection [41].

2.6. Image analysis and statistics

Following raw data acquisition, sagittal cross-sections were examined in ImageJ to determine the penetration of contrast agent and quantify pocket depths. First, images were converted to 8-bit images and exported as two files: one that displayed only the photoacoustic signal and another that displayed only the ultrasound. For these images, a line profile was manually drawn parallel to the gingival margin through both images (Fig. S2). From this, the pixel intensity could be plotted with respect to the position along the line for both the photoacoustic and ultrasound images. Then, a minimum pixel intensity of 4% was used as a threshold, above which signal was considered significant. If both signals were above the threshold at a given position, then that point was considered part of the pocket depth. Taken together, all of these points formed a length and its magnitude was recorded as the pocket depth.

To avoid bias during quantitative comparison to physical probing, sagittal planes were chosen the same way each time: for distobuccal and mesiobuccal sites, we chose the first 8 sagittal planes (0.6 mm-wide sections) with a measurable pocket depth on each lateral side of the tooth. These sections mimicked the diameters of the physical probes. For the buccal sites, we selected 0.6 mm-wide sections from the images at the deepest part of the pocket. This dimension mimicked the diameter of the physical probes and the typical procedure of recording the lowest number obtained by walking the probe across the pocket width. For replicate measurements, images were collected on nonconsecutive days across two weeks.

The buccal contours of the pocket geometry were mapped by averaging five separate imaging events. The width of the pocket consisted of dozens of sagittal planes. For each plane, two measurements were taken: the distance from the crown of the tooth to the gingival margin, and the distance from the gingival margin to the edge of

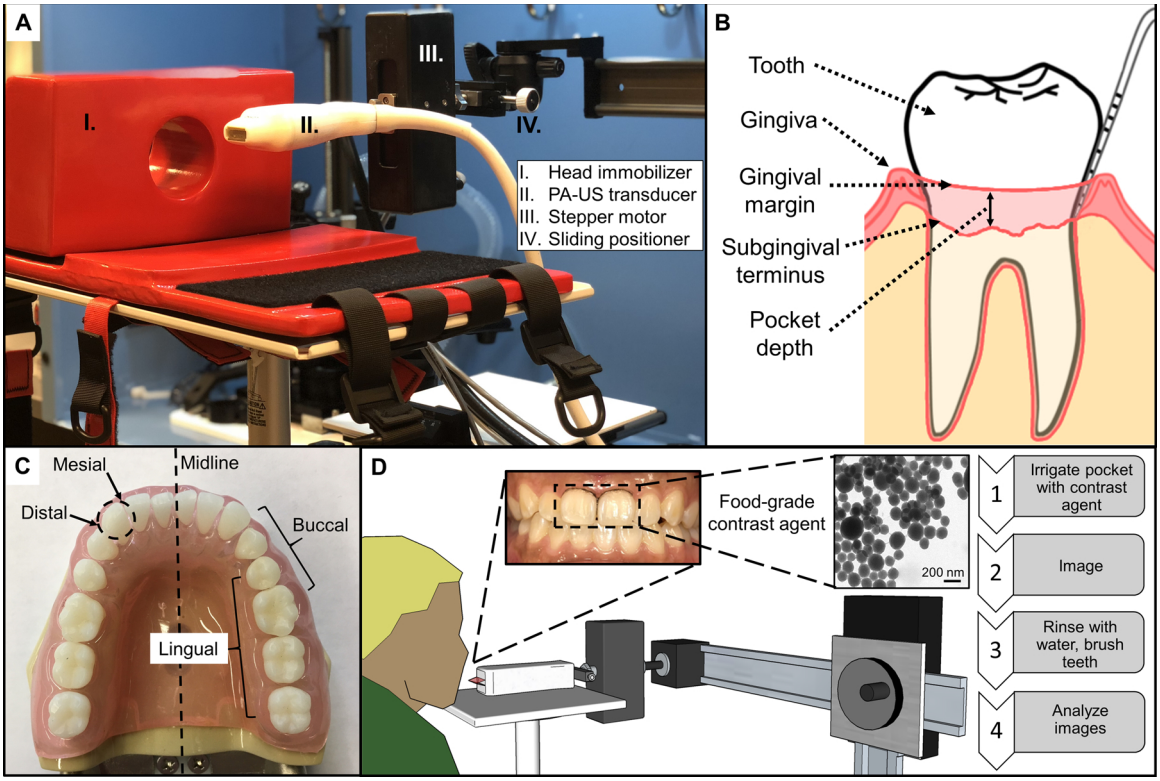

Fig. 1. Overview of the imaging setup, periodontal anatomy, and workflow. (**A**) The PA-US transducer was connected to a stepper motor for axial scanning and a sliding positioner for lateral control—these components were attached to a larger frame for general positioning. The head immobilizer (cross-section shown) rested on a flat surface. (**B**) The simplified diagram shows a tooth, gingiva, gingival margin, subgingival terminus, and pocket depth for an arbitrary cross-section. (**C**) Anatomical terms for periodontal reference: Mesial refers to a location on a tooth that is closer to the midline while distal refers to one that is further. Lingual refers to the side of a tooth facing the tongue while buccal refers to the side facing the cheek. For example, mesiobuccal and distobuccal refer to the areas of the buccal face of a tooth that are closer to and farther from the midline of the mouth, respectively. (**D**) Experimental workflow. Briefly, a contrast agent containing melanin nanoparticles (TEM inset) derived from cuttlefish ink was used to irrigate the pocket of a target tooth followed by photoacoustic imaging. The pocket could be rinsed with water and then images could be analyzed to measure pocket depths.

photoacoustic signal (the subgingival terminus). Together, these measurements determined the top and bottom of the pocket for that plane. Once these measurements were taken for all planes, they were used to reconstruct a full map of the pocket to overlap on top of the ultrasound image.

3. Results

3.1. High-resolution ultrasound imaging of teeth and soft tissues

Photoacoustic and ultrasound images were collected by adapting a commercial PA-US system for human operation (Fig. 1). Ultrasound imaging was used to generate frontal and sagittal cross-sections of 10 teeth (tooth numbers 7–10, 22–27) and their associated soft tissues from a healthy volunteer (Fig. 2). They were labelled with the numbering system used by the American Dental Association [42]. These anterior teeth were imaged because the size of the transducer limited access to the posterior region of the oral cavity.

Increasing the ultrasound transducer frequency (Fig. 2A) significantly improved our ability to identify the gingival margin. The spatial resolution of the ultrasound mode was approximately 100 μm at 40 MHz and 300 μm for the photoacoustic mode [22,43]. At 15 and 21 MHz, the gingival-tooth interface and subgingival tooth could not be identified. These features were clearly resolved at 40 MHz, and we used this frequency for all subsequent images. Frontal views captured surface features of the teeth and tissue, while sagittal views revealed the gingival margin, gingival thickness, and surface topology (Fig. 2B).

3.2. Periodontal labeling and photoacoustic imaging

The contrast agent possessed broad photoacoustic absorption from 680 to 970 nm due to the presence of melanin nanoparticles (Fig. S1) [22,44,45]. Following administration of contrast agent, we collected PA-US images and overlaid the 680-nm signal on ultrasound to measure the periodontal pocket depths. Frontal and sagittal views of the lower central incisors in Fig. 3A–D show the signal from the mid-buccal pocket after applying the contrast agent and imaging. The mid-buccal pocket depth of tooth number 25 was 1.31 mm (Fig. 3D); signal from the supragingival surface of the tooth did not contribute to the measurement. The gingival thickness could also be quantified. When measured at the mid-buccal plane, 2 mm below the gingival margin, the gingival thickness was 1.01 ± 0.05 mm for tooth 25 and 0.97 ± 0.04 mm for tooth 24 (n = 5). These values matched the average thickness reported for a 16–24 year old age group [46].

To demonstrate reproducibility, we conducted five independent replicates by performing the entire labelling, imaging, cleaning, and processing procedure from start to finish on different days (Fig. S2). In Fig. 3E–F, the pocket depths are plotted across these replicates for buccal, mesiobuccal, and distobuccal planes. The means and standard deviations for these locations were 1.24 ± 0.04 mm, 0.74 ± 0.12 mm, and 0.68 ± 0.06 mm respectively. These corresponded to relative standard deviations of 3%, 16%, and 9%.

The pocket depth could be determined for a single plane, a region of planes, or the full buccal width of the pocket. The distance between each plane was 0.076 mm, corresponding to roughly 50–120 measurements per tooth. Fig. 4 shows the steps to construct a visualization of the full pocket overlaid on a frontal US image of the tooth. The

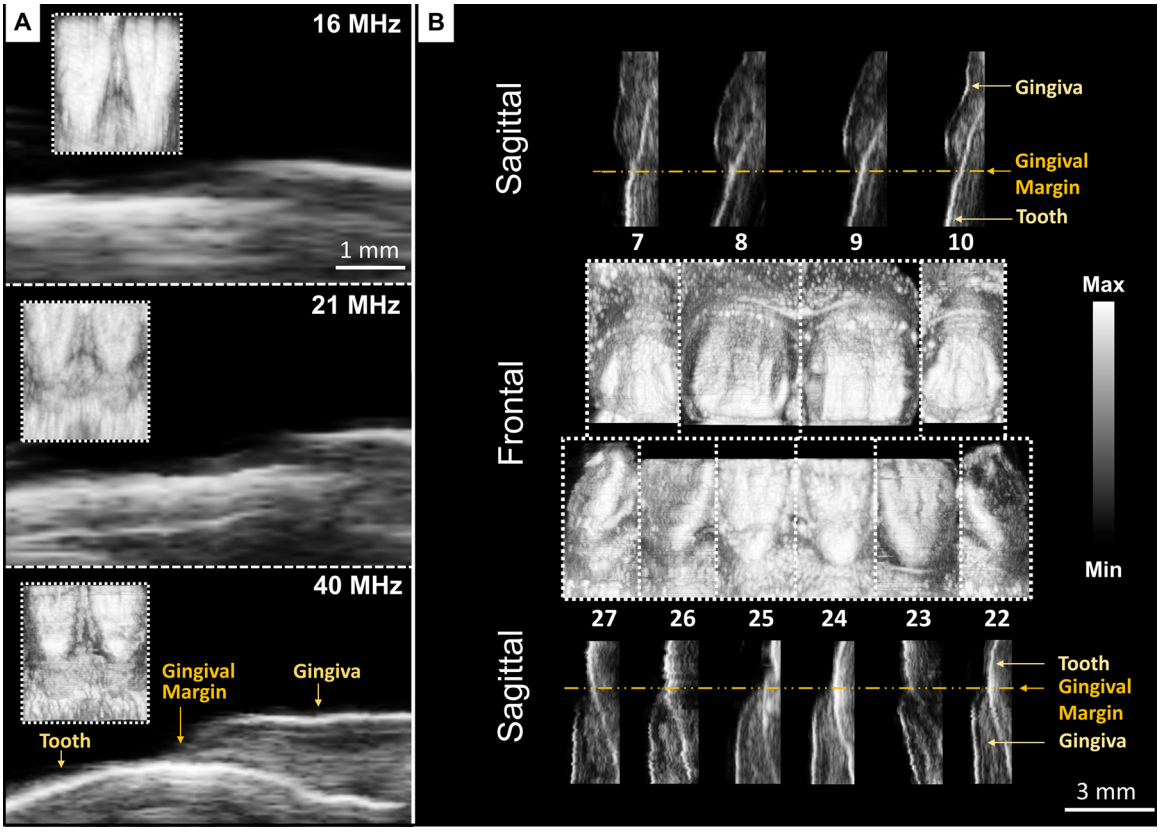

Fig. 2. US images of ten teeth acquired from one subject at 40 MHz and comparison to images at lower frequencies. (**A**) Frontal and sagittal images of the bottom front incisors (24 and 25) at increasing US frequencies. Frontal images are inset within the magnified sagittal images of tooth 25 at the gingival margin. Scale bars are 1 mm and apply to all frequencies for the sagittal images. (**B**) Frontal and sagittal cross-sections of teeth 7–10 and 22–27. The frontal and sagittal views are composites of planes from ten separate scans. The gingiva, gingival margin, and tooth are resolved in each sagittal image. The 3-mm scale bar is for sagittal images.

measurements for these steps were performed five times (n = 5) on a lower central incisor across its measurable width (Fig. 4A–B). The total mean for the full pocket width was 1.02 ± 0.21 mm. The mean standard deviation of these measurements, i.e. the average of the standard deviations for every measurement plane across five replicates, was 0.104 mm, resulting in a relative standard deviation of 10.2% (Fig. 4E). Furthermore, the range of the measurements was 0.57 mm, reflecting the variation in pocket depth according to probing location. The distobuccal, buccal, and mesiobuccal regions of planes (0.6 mm wide each) had measurements of 0.84 ± 0.17 mm, 1.15 ± 0.05, and 0.79 ± 0.05. Fig. 4C shows a sagittal plane from Fig. 4B split into photoacoustic and ultrasound signal only with a line profile drawn

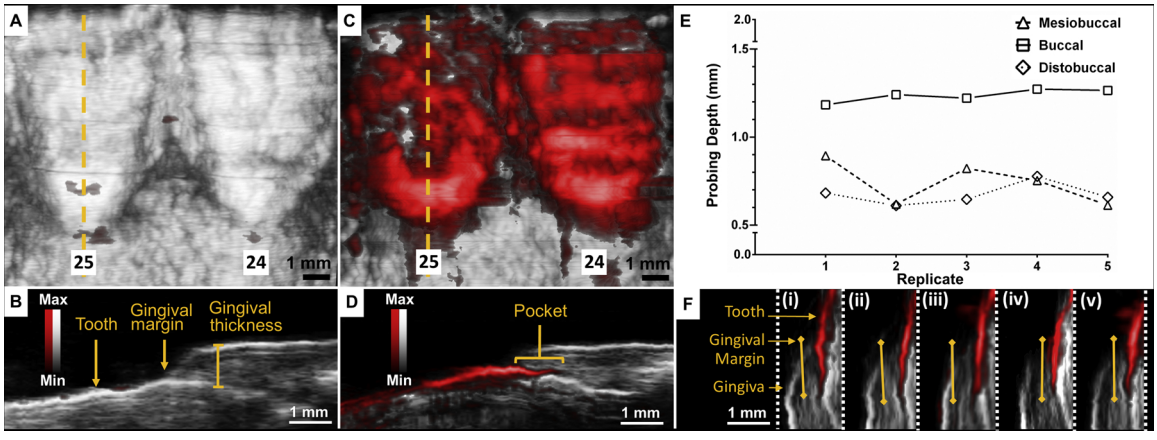

Fig. 3. Photoacoustic-ultrasound images of the bottom front incisors (24, 25) before and after administration of contrast agent with demonstrated reproducibility. (**A**) Frontal cross-section of teeth 24 and 25 with photoacoustic signal overlaid on ultrasound prior to administration of contrast agent. (**B**) Sagittal cross-section of tooth 25, indicated by the dashed yellow line in Panel **A**, with tooth, gingival margin, and gingival thickness labelled. (**C**) Frontal cross-section of teeth 24 and 25 with photoacoustic signal overlaid on ultrasound after administration of contrast agent. (**D**) The sagittal cross-section of tooth 25 (dashed yellow line in Panel **C**) shows the soft-hard tissue interface and pocket revealed by the photoacoustic contrast agent below the gingival margin. (**E, F**) Reproducibility of measurements for representative sagittal planes at mesiobuccal, central buccal, and distobuccal probing locations across five replicates in tooth 25; labeling and imaging procedures were performed independently from beginning to end. Each PA-US image in **F** corresponds to the mesiobuccal probing depth measurement (squares) for its given replicate number on the x-axis in **E**. Light yellow lines show the pocket measurements. White: ultrasound, red: photoacoustic.

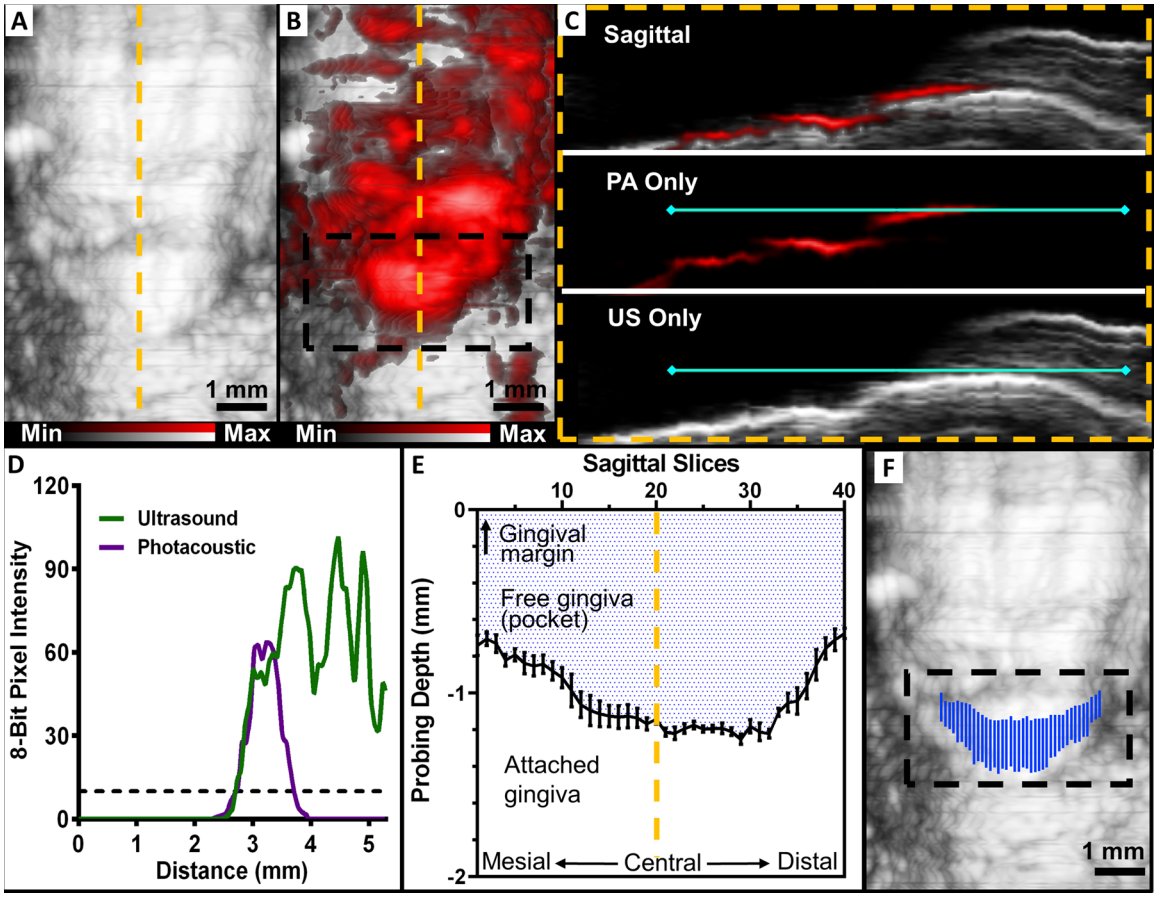

Fig. 4. Procedure for mapping the full width and contours of the periodontal pocket. (**A**) US frontal image of tooth 25 prior to administration of contrast agent. (**B**) PA-US frontal image of the same tooth following contrast agent with the subgingival region of interest highlighted by a black box, prior to image processing. (**C**) A sagittal view of the tooth at the yellow dashed line from (A) and (B) used for image processing. The top of panel C is an overlay and the lower panels are ultrasound and photoacoustic layers. A line (solid turquoise) was manually drawn parallel to the gingival margin for both of the layers using ImageJ. (**D**) The 8-bit pixel intensities of the ultrasound and photoacoustic signal along the line were plotted with respect to the length of the line. A minimum intensity threshold (dashed line) of 10 was chosen to minimize the influence of background signal, and the pocket depth was taken as the total length for which the photoacoustic and ultrasound signals were both higher than the threshold, i.e., from 2.71 mm to 3.72 mm. (**E**) Pocket measurements for every sagittal plane across the full buccal width of the tooth– a total of 40 planes were measured. The x-axis represents each sagittal slice across the width of the tooth. The shaded region represents the geometry of the pocket and the white region represents the normal area of attachment between tooth and epithelia. Error bars show the standard error of the mean for five replicates (n = 5). (**F**) The final mapping of the pocket generated by our photoacoustic method. It was generated by taking the measurements for each sagittal slice from (**E**) and overlaying them on the ultrasound image. This step removes the non-specific photoacoustic signal from (**B**).

parallel to the gingival margin. Fig. 4D quantifies the intensity of each signal along the line profile, which indicates a pocket depth of 1.01 mm for the plane. The final mapping of the pocket geometry is shown overlaid on the ultrasound image in Fig. 4F.

We evaluated the persistence of contrast agent in the pockets following oral rinses with water as well as brushing (Fig. 5). The reduction of pocket measurements was averaged from six representative planes across teeth 24 and 25 following 15 s rinsing, 30 s rinsing, and brushing; these steps resulted in 12.5%, 25.2%, and 100% reductions respectively when averaged across five replicates.

Finally, we compared our pocket measurements with the gold standard (Williams and Marquis) probes. The lowest possible measurement from the probes, as determined by a periodontist, was 2 mm (any lower values were rounded up); this value was recorded for the buccal pockets of teeth 24 and 25 with both probes. We measured 1.34 mm and 1.15 mm (n = 5) for teeth numbers 24 and 25 with PA-US, respectively, which agreed with the gold standard measurements while providing more precision.

4. Discussion

We report the first application of PA imaging for monitoring dental and periodontal health in humans by using a food-grade contrast agent. This technique is ideal for imaging periodontal pockets, gingival soft tissue and thickness, and the surfaces of teeth. These features could be distinguished both by visual inspection— ultrasound signal from tooth is brighter than tissue— and more quantitatively with line profiles of photoacoustic and ultrasound pixel intensities (Fig. 4D, Fig. S2). We determined that a 40 MHz ultrasound frequency provided sufficient resolution for discerning these features without sacrificing the requisite penetration depth. The US-only mode is particularly suited for applications that require knowledge of how a tooth is situated within the gingiva—one potential example would be diagnosis and monitoring of patients with delayed tooth eruption [47].

The flow of contrast agent into the gingival sulcus allowed the imaging and measurement of pocket depths, eliminating the need for probing. In the case of patients with peri-implantitis, this technique has potential to allow pocket depth measurements when physical probing is risky or impossible due to threading along the implant surface and tissue sensitivity. It was common for the agent to coat the majority of the tooth surface even when it was locally administered to the gingival margin (Fig. 3A); however, this did not adversely affect measurements. The beginning of the pocket could always be identified by overlaying the ultrasound image to reveal the gingival margin and gingival

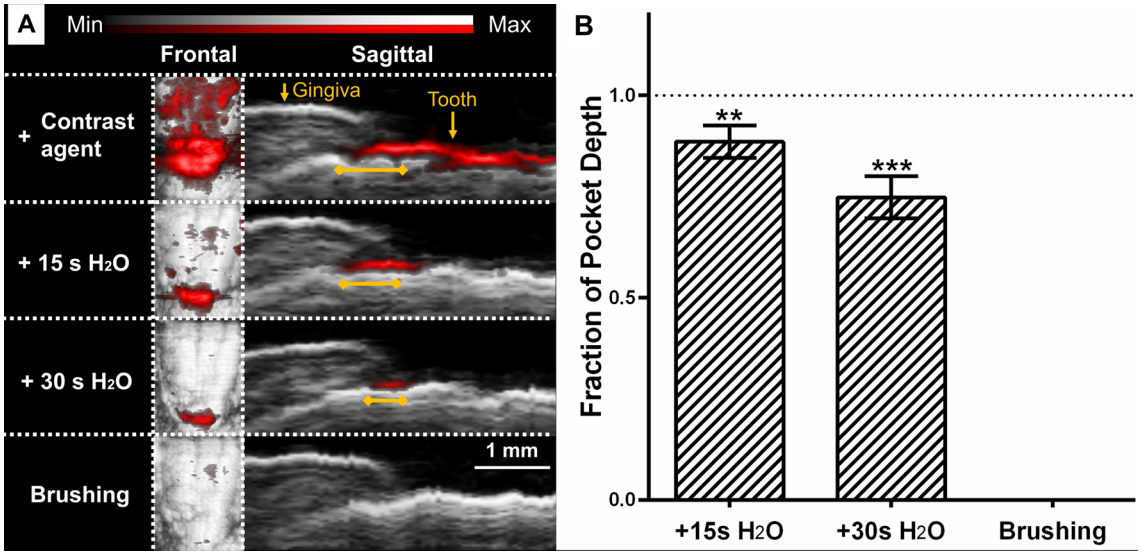

Fig. 5. Removal of contrast agent following oral rinsing with water and teeth brushing. (**A**) Representative PA-US images show the reduction in photoacoustic signal/pocket measurement following oral rinsing with water for 15 s, 30 s, and brushing. Yellow lines indicate the pocket measurements. (**B**) Fraction of original measurement following washing steps for five representative sagittal planes taken from teeth 24 and 25. The dotted line indicates the original measurement and error bars show SEM (n = 5). Asterisks denote significant difference from original measurement (unpaired t-test), ** ($P \leq 0.01$), *** ($P \leq 0.001$).

thickness (Fig. 3B). The imaging procedure took roughly 5 min per tooth but could be greatly improved with a mouthpiece transducer capable of scanning all teeth at once.

The PA imaging technique is highly reproducible (Figs. 3E, 4 E) with relative standard deviations of 10%. This precision offers a major improvement over the Williams probe, which can only record integer values for pocket depths and has inter-operator error of up to 40% [48]. The periodontal pocket is a dynamic structure due to the constant battle between bacterial invasion and the immune response [49], and integers are a poor reflection of this process. In a typical oral exam, six measurements are taken per tooth (distolingual, lingual, mesiolingual, distobuccal, buccal, and mesiobuccal) to approximate the full profile of the pocket [14]. We show that photoacoustic imaging can be used to reveal the entirety of the buccal pocket with sub-millimeter (0.01 mm) precision (Fig. 4). The overlay in Fig. 4F was created manually but it represents a convenient visualization tool for clinicians; in the future, the conversion from raw data to final image with highlighted pocket would be performed by automated algorithms [50]. Imaging the whole pocket over the patients' lifetimes has previously been impossible and could supersede periodontal charting— this practice could reveal the development of abnormalities that would otherwise be overlooked.

We observed that contrast agent could be easily removed from the gingival sulcus after imaging (Fig. 5). Oral rinsing with water reduced the contrast agent both on the surface of the teeth and within the sulcus; a few seconds of normal brushing completely removed the agent. We saw that our PA-US measurements (#24 = 1.34 mm, #25 = 1.17 mm) were in good agreement with those acquired by the Williams and Marquis probes, which recorded 2 mm for both lower central incisors. The probes were not capable of distinguishing any values lower than 2 mm; in addition, they could only record integers and relied on subjective estimation. PA-US imaging lowers ambiguity and improves the precision of measurements.

We recognize some limitations in this study. Due to the size of the PA—US transducer, only anterior teeth could be imaged. In principle, all 32 teeth and the periodontium can be imaged with this technique but the geometry of our PA—US transducer physically limited access. Fortunately, several groups have reported custom transducer geometries, and future work includes development of a mouthpiece-shaped device to overcome this limitation [51–53]. A mouthpiece transducer would also reduce imaging artifacts caused by motion from the subject during scanning because the subject could bite down on the device. Partial penetration of contrast agent into the sulcus is also a possibility but the extent of penetration is consistent across irrigation and scanning events (Fig. 3C). The subject of the study had good oral hygiene and did not have deep (≥ 4 mm) pockets indicative of periodontal disease. However, we previously showed that deep pockets could be imaged in swine, a good model of the human gingiva [22,54]. Finally, because the periodontal pocket is a dynamic structure, imaging and probing across different days may have contributed to small variations in measurements.

5. Conclusion

This work demonstrates the first use of photoacoustic imaging for monitoring periodontal health in humans by quantitating pocket depths. The measurements acquired with this technique agreed with those acquired by a trained periodontist, while providing significantly more spatial information and precision. The gold-standard periodontal probe is an established but limited tool. This technique presents an opportunity for dental clinicians to move away from manual probing and toward photoacoustic image-guided diagnostics. Ultimately, we envision the development of a compact, PA-US mouthpiece as a platform for fast, non-invasive collection of critical periodontal metrics.

Conflicts of interest

The authors declare that there are no conflicts of interest regarding the authorship and publication of this article.

Acknowledgements

We acknowledge support from the National Institutes of Health through DP2 HL 137187, S10 OD 021821 and T32 EB009380.

Appendix A. Supplementary data

Supplementary material related to this article can be found, in the online version, at doi:https://doi.org/10.1016/j.pacs.2018.10.005.

References

[1] P.I. Eke, B. Dye, L. Wei, G. Thornton-Evans, R. Genco, Prevalence of periodontitis in adults in the United States: 2009 and 2010, J. Dent. Res. 91 (10) (2012) 914–920.
[2] F. D'aiuto, L. Nibali, M. Parkar, K. Patel, J. Suvan, N. Donos, Oxidative stress, systemic inflammation, and severe periodontitis, J. Dent. Res. 89 (11) (2010) 1241–1246.
[3] R.P. Darveau, Periodontitis: a polymicrobial disruption of host homeostasis, Nat. Rev. Microbiol. 8 (7) (2010) 481.
[4] D.L. Cochran, Inflammation and bone loss in periodontal disease, J. Periodontol. 79 (8S) (2008) 1569–1576.
[5] H. Karadottir, L. Lenoir, B. Barbierato, M. Bogle, M. Riggs, T. Sigurdsson, M. Crigger, J. Egelberg, Pain experienced by patients during periodontal maintenance treatment, J. Periodontol. 73 (5) (2002) 536–542.
[6] M.S. Tonetti, T.E. Dyke, Periodontitis and atherosclerotic cardiovascular disease: consensus report of the Joint EFP/AAP Workshop on Periodontitis and Systemic Diseases, J. Clin. Periodontol. 40 (s14) (2013).
[7] R. Stewart, M. West, Increasing evidence for an association between periodontitis and cardiovascular disease, Am. Heart Assoc. 133 (6) (2016) 549–551.
[8] W.-D. Leng, X.-T. Zeng, J.S. Kwong, X.-P. Hua, Periodontal disease and risk of coronary heart disease: an updated meta-analysis of prospective cohort studies, Int. J. Cardiol. 201 (2015) 469–472.
[9] D. Michaud, K. Kelsey, E. Papathanasiou, C. Genco, E. Giovannucci, Periodontal disease and risk of all cancers among male never smokers: an updated analysis of the Health Professionals Follow-up Study, Ann. Oncol. 27 (5) (2016) 941–947.
[10] Y.T. Lee, H.C. Lee, C.J. Hu, L.K. Huang, S.P. Chao, C.P. Lin, E.C.Y. Su, Y.C. Lee, C.C. Chen, Periodontitis as a modifiable risk factor for dementia: a nationwide population-based cohort study, J. Am. Geriatr. Soc. 65 (2) (2017) 301–305.
[11] K. Abbayya, N.Y. Puthanakar, S. Naduwinmani, Y. Chidambar, Association between periodontitis and Alzheimer's disease, N. Am. J. Med. Sci. 7 (6) (2015) 241.
[12] K.S. Kornman, Mapping the pathogenesis of periodontitis: a new look, J. Periodontol. 79 (8S) (2008) 1560–1568.
[13] A. Mariotti, A.F. Hefti, Defining periodontal health, BMC oral health, BioMed Central (2015) S6.
[14] D. Perry, Periodontology for the Dental Hygienist, 4 ed., Elsevier, St. Louis, MO, 2014.
[15] S.G. Grossi, R.G. Dunford, A. Ho, G. Koch, E.E. Machtei, R.J. Genco, Sources of error for periodontal probing measurements, J. Periodont. Res. 31 (5) (1996) 330–336.
[16] C. Larsen, D.S. Barendregt, D.E. Slot, U. Van der Velden, F. Van der Weijden, Probing pressure, a highly undervalued unit of measure in periodontal probing: a systematic review on its effect on probing pocket depth, J. Clin. Periodontol. 36 (4) (2009) 315–322.
[17] G.C. Armitage, G.K. Svanberc, H. Löe, Microscopic evaluation of clinical measurements of connective tissue attachment levels, J. Clin. Periodontol. 4 (3) (1977) 173–190.
[18] S. Koka, The implant-mucosal interface and its role in the long-term success of endosseous oral implants: a review of the literature, Int. J. Prosthodont. 11 (5) (1999) 421–432.
[19] S. Schou, P. Holmstrup, K. Stoltze, E. Hjørting-Hansen, N.-E. Fiehn, L.T. Skovgaard, Probing around implants and teeth with healthy or inflamed peri-implant mucosa/gingiva, Clin. Oral Implants Res. 13 (2) (2002) 113–126.
[20] V.M. Giraldo, A. Duque, A.G. Aristizabal, R.D.M. Hernández, Prevalence of peri-implant disease according to periodontal probing depth and bleeding on probing: a systematic review and meta-analysis, Int. J. Oral Maxillofac. Implants 33 (4) (2018) e89–e105.
[21] M. Rakic, P. Galindo-Moreno, A. Monje, S. Radovanovic, H.-L. Wang, D. Cochran, A. Sculean, L. Canullo, How frequent does peri-implantitis occur? A systematic review and meta-analysis, Clin. Oral Investig. 22 (4) (2018) 1805–1816.
[22] C. Lin, F. Chen, A. Hariri, C. Chen, P. Wilder-Smith, T. Takesh, J. Jokerst, Photoacoustic imaging for noninvasive periodontal probing depth measurements, J. Dent. Res. (2017) 0022034517729820.
[23] L.V. Wang, S. Hu, Photoacoustic tomography: in vivo imaging from organelles to organs, Science 335 (6075) (2012) 1458–1462.
[24] J.E. Lemaster, J.V. Jokerst, What is new in nanoparticle-based photoacoustic imaging? Wiley Interdiscip. Rev. Nanomed. Nanobiotechnol. 9 (1) (2017).
[25] M. Xu, L.V. Wang, Photoacoustic imaging in biomedicine, Rev. Sci. Instrum. 77 (4) (2006) 041101.
[26] A. Stylogiannis, L. Prade, A. Buehler, J. Aguirre, G. Sergiadis, V. Ntziachristos, Continuous wave laser diodes enable fast optoacoustic imaging, Photoacoustics 9 (2018) 31–38.
[27] P. Beard, Biomedical Photoacoustic Imaging, Interface Focus, (2011) rsfs20110028.
[28] X.L. Deán-Ben, D. Razansky, Optoacoustic signal excitation with a tone-burst of short pulses, Photoacoustics 11 (2018) 1–5.
[29] S. Zackrisson, S. Van De Ven, S. Gambhir, Light in and sound out: emerging translational strategies for photoacoustic imaging, Cancer Res. 74 (4) (2014) 979–1004.
[30] S. Mallidi, G.P. Luke, S. Emelianov, Photoacoustic imaging in cancer detection, diagnosis, and treatment guidance, Trends Biotechnol. 29 (5) (2011) 213–221.
[31] F. Knieling, C. Neufert, A. Hartmann, J. Claussen, A. Urich, C. Egger, M. Vetter, S. Fischer, L. Pfeifer, A. Hagel, C. Kielisch, R.S. Görtz, D. Wildner, M. Engel, J. Röther, W. Uter, J. Siebler, R. Atreya, W. Rascher, D. Strobel, M.F. Neurath, M.J. Waldner, Multispectral optoacoustic tomography for assessment of Crohn's disease activity, N. Engl. J. Med. 376 (13) (2017) 1292–1294.
[32] J. Jo, C. Tian, G. Xu, J. Sarazin, E. Schiopu, G. Gandikota, X. Wang, Photoacoustic tomography for human musculoskeletal imaging and inflammatory arthritis detection, Photoacoustics (2018).
[33] M. Masthoff, A. Helfen, J. Claussen, et al., Use of multispectral optoacoustic tomography to diagnose vascular malformations, JAMA Dermatol. (2018) 1–6.
[34] J. Aguirre, B. Hindelang, A. Berezhnoi, U. Darsow, F. Lauffer, K. Eyerich, T. Biedermann, V. Ntziachristos, Assessing nailfold microvascular structure with ultra-wideband raster-scan optoacoustic mesoscopy, Photoacoustics 10 (2018) 31–37.
[35] A.B.E. Attia, S.Y. Chuah, D. Razansky, C.J.H. Ho, P. Malempati, U.S. Dinish, R. Bi, C.Y. Fu, S.J. Ford, J.S.-S. Lee, M.W.P. Tan, M. Olivo, S.T.G. Thng, Noninvasive real-time characterization of non-melanoma skin cancers with handheld optoacoustic probes, Photoacoustics 7 (2017) 20–26.
[36] B. Vandenberghe, R. Jacobs, H. Bosmans, Modern dental imaging: a review of the current technology and clinical applications in dental practice, Eur. Radiol. 20 (11) (2010) 2637–2655.
[37] D.C. Barratt, C.S. Chan, P.J. Edwards, G.P. Penney, M. Slomczykowski, T.J. Carter, D.J. Hawkes, Instantiation and registration of statistical shape models of the femur and pelvis using 3D ultrasound imaging, Med. Image Anal. 12 (3) (2008) 358–374.
[38] F.C. Pekam, J. Marotti, S. Wolfart, J. Tinschert, K. Radermacher, S. Heger, High-frequency ultrasound as an option for scanning of prepared teeth: an in vitro study, Ultrasound Med. Biol. 41 (1) (2015) 309–316.
[39] E.D. Samuel, G.S. Griffiths, A. Petrie, In vitro accuracy and reproducibility of automated and conventional periodontal probes, J. Clin. Periodontol. 24 (5) (1997) 340–345.
[40] A. Savage, K.A. Eaton, D.R. Moles, I. Needleman, A systematic review of definitions of periodontitis and methods that have been used to identify this disease, J. Clin. Periodontol. 36 (6) (2009) 458–467.
[41] E.K. Fishman, D.R. Ney, D.G. Heath, F.M. Corl, K.M. Horton, P.T. Johnson, Volume rendering versus maximum intensity projection in CT angiography: what works best, when, and why, Radiographics 26 (3) (2006) 905–922.
[42] E.F. Harris, Tooth-coding systems in the clinical dental setting, Dent. Anthropol. J. 18 (2) (2005) 43–49.
[43] C.M. Moran, S.D. Pye, W. Ellis, A. Janeczko, K.D. Morris, A.S. McNeilly, H.M. Fraser, A comparison of the imaging performance of high resolution ultrasound scanners for preclinical imaging, Ultrasound Med. Biol. 37 (3) (2011) 493–501.
[44] A. Liopo, R. Su, A.A. Oraevsky, Melanin nanoparticles as a novel contrast agent for optoacoustic tomography, Photoacoustics 3 (1) (2015) 35–43.
[45] Q. Fan, K. Cheng, X. Hu, X. Ma, R. Zhang, M. Yang, X. Lu, L. Xing, W. Huang, S.S. Gambhir, Z. Cheng, Transferring biomarker into molecular probe: melanin nanoparticle as a naturally active platform for multimodality imaging, J. Am. Chem. Soc. 136 (43) (2014) 15185–15194.
[46] K.L. Vandana, B. Savitha, Thickness of gingiva in association with age, gender and dental arch location, J. Clin. Periodontol. 32 (7) (2005) 828–830.
[47] L. Suri, E. Gagari, H. Vastardis, Delayed tooth eruption: pathogenesis, diagnosis, and treatment. A literature review, Am. J. Orthodontics Dentofacial Orthopedics 126 (4) (2004) 432–445.
[48] M.A. Listgarten, Periodontal probing: what does it mean? J. Clin. Periodontol. 7 (3) (1980) 165–176.
[49] M.G. Newman, H. Takei, P.R. Klokkevold, F.A. Carranza, Carranza's clinical periodontology, Elsevier Health Sci. (2011) 127–139 11th ed..
[50] T. Lehmann, E. Troeltsch, K. Spitzer, Image processing and enhancement provided by commercial dental software programs, Dentomaxillofacial Radiol. 31 (4) (2002) 264–272.
[51] M.A.L. Bell, N.P. Kuo, D.Y. Song, J.U. Kang, E.M. Boctor, In vivo visualization of prostate brachytherapy seeds with photoacoustic imaging, J. Biomed. Opt. 19 (12) (2014) 126011–126011.
[52] A. Nikoozadeh, C. Chang, J.W. Choe, A. Bhuyan, B.C. Lee, A. Moini, P.T. Khuri-Yakub, An integrated ring CMUT array for endoscopic ultrasound and photoacoustic imaging, ultrasonics symposium (IUS), 2013 IEEE International, IEEE, (2013), pp. 1178–1181.
[53] J.-M. Yang, C.P. Favazza, J. Yao, R. Chen, Q. Zhou, K.K. Shung, L.V. Wang, Three-dimensional photoacoustic and ultrasonic endoscopic imaging of two rabbit esophagi, SPIE BiOS, Int. Soc. Optics Photonics (2015) pp. 932334-932334-8.
[54] S. Wang, Y. Liu, D. Fang, S. Shi, The miniature pig: a useful large animal model for dental and orofacial research, Oral Dis. 13 (6) (2007) 530–537.

Colman Moore, BS, is a PhD student in the Nanoengineering department at UC San Diego. He graduated from the University of South Carolina Honors College with a B.S. in Biomedical Engineering. He is interested in the development of novel bio-imaging applications and the intersection of engineered contrast agents with noninvasive imaging modalities.

Yuting Bai, BA, is a visiting scholar in the NanoEngineering department at UC San Diego. She graduated from Wesleyan College with a B.A. in Biology and Chemistry and is pursuing an MBID in Biomedical Innovation and Development at Georgia Tech.

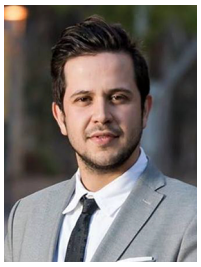

Ali Hariri, BS, MS, is a PhD student in the Nanoengineering Department at UCSD. He got his M.S. degree and B.S degree in Biomedical Engineering from Sharif University of Technology and Amirkabir University of Technology in Iran. He has worked on developing various configurations of photoacoustic imaging, including LED systems, computed tomography, and microscopy (both acoustic and optical resolution).

Joan Beleno Sanchez, RDH, BSDH, BAS, is a clinical instructor and a member of the periodontal endoscope faculty in the Department of Dental Hygiene at the USC Ostrow School of Dentistry. She also works in private clinical practice and as a research coordinator.

Ching-Yu Lin, MS, is a visiting graduate student in the NanoEngineering department at UC San Diego. She got her M.S. degree in Biomedical Engineering from National Cheng Kung University in Taiwan.

Sreenivas Koka, DDS, PhD, MBA is a lecturer at the University of California, Los Angeles and owns his own dental clinic in San Diego as a specialist dentist and prosthodontist. He received his Doctorate of Dental Surgery from the University of Michigan and his Ph.D. in Oral Biology from the University of Nebraska. In 2013, he completed a Master's in Business Administration from the Sloan School of Management at Massachusetts Institute of Technology. Dr. Koka has previously served as Consultant in Prosthodontics at the Mayo Clinic, the Executive Director of the Foundation for Oral Rehabilitation in Zurich, Switzerland, and is a recipient of the Clinician-Researcher Award from the American College of Prosthodontists.

Parish Sedghizadeh, DDS, QME, is an Assistant Professor at the University of Southern California, Ostrow School of Dentistry, and Director of the USC Center for Biofilms. He received his Bachelor of Science degree in biology from UCLA, and his Doctorate of Dental Surgery from USC. After his doctorate, he pursued specialty training in Oral and Maxillofacial Pathology at Ohio State University, where he also attained a Master of Science degree in oral biology and fellowship status in the American Academy of Oral and Maxillofacial Pathology. Dr. Sedghizadeh conducts research, publishes, consults and teaches oral pathology, radiology and medicine and has an active clinical practice at USC.

Casey Chen, BDS, PhD, DDS, is Professor and Co-chair of the Division of Primary Oral Health Care at the Herman Ostrow School of Dentistry of USC. He graduated from the National Taiwan University with a degree of BDS, has obtained a certificate in Periodontology at the University of Pittsburgh, a Ph.D. in Oral Biology from the State University of New York at Buffalo, and a dental degree from Loma Linda University. Dr. Chen also maintains a private practice limited to periodontics in Irvine, California.

Jesse Jokerst, PHD, is an Assistant Professor at the University of California San Diego. He received a B.S. in chemistry from Truman State University and his Ph.D. in chemistry from the University of Texas at Austin with John T. McDevitt. Dr. Jokerst completed his postdoctoral training with Sanjiv Gambhir at Stanford University in the Department of Radiology, where he developed novel ultrasound and photoacoustic molecular imaging approaches to study ovarian cancer and monitor stem cell therapy. His current research emphasizes photoacoustic and ultrasound imaging, novel contrast agents for hybrid imaging techniques, and wearable sensors.